

Chemical Tagging N-rich Field Stars with High-resolution Spectroscopy

JINCHENG YU,¹ BAITIAN TANG,¹ J. G. FERNANDEZ-TRINCADO,^{2,3} DOUGLAS GEISLER,^{4,5,6} HONGLIANG YAN,⁷ AND
M. SOTO²

¹*School of Physics and Astronomy, Sun Yat-sen University, Zhuhai 519082, China*

²*Instituto de Astronomía y Ciencias Planetarias, Universidad de Atacama, Copayapu 485, Copiapó, Chile*

³*Centro de Investigación en Astronomía, Universidad Bernardo O Higgins, Avenida Viel 1497, Santiago, Chile*

⁴*Departamento de Astronomía, Casilla 160-C, Universidad de Concepción, Concepción, Chile*

⁵*Instituto de Investigación Multidisciplinario en Ciencia y Tecnología, Universidad de La Serena. Avenida Raúl Bitrán S/N, La Serena, Chile*

⁶*Departamento de Astronomía, Facultad de Ciencias, Universidad de La Serena. Av.*

⁷*Key Lab of Optical Astronomy, National Astronomical Observatories, Chinese Academy of Sciences, 20A Datun Road, Beijing 100101, China*

ABSTRACT

We measure chemical abundances for over 20 elements of 15 N-rich field stars with high resolution ($R \sim 30000$) optical spectra. We find that Na, Mg, Al, Si, and Ca abundances of our N-rich field stars are mostly consistent with those of stars from globular clusters (GCs). Seven stars are estimated to have $[\text{Al}/\text{Fe}] > 0.5$, which is not found in most GC “first generation” stars. On the other hand, α element abundances (especially Ti) could show distinguishable differences between in situ stars and accreted stars. We discover that one interesting star, with consistently low $[\text{Mg}/\text{Fe}]$, $[\text{Si}/\text{Fe}]$, $[\text{Ca}/\text{Fe}]$, $[\text{Ti}/\text{Fe}]$, $[\text{Sc}/\text{Fe}]$, $[\text{V}/\text{Fe}]$, and $[\text{Co}/\text{Fe}]$, show similar kinematic and $[\text{Ba}/\text{Eu}]$ as other stars from the dissolved dwarf galaxy “*Gaia*-Sausage-Enceladus”. The α -element abundances and the iron-peak element abundances of the N-rich field stars with metallicities $-1.25 \leq [\text{Fe}/\text{H}] \leq -0.95$ show consistent values with Milky Way field stars ^{a)} rather than stars from dwarf galaxies, indicating that they were formed in situ. In addition, the neutron capture elements of N-rich field stars show that most of them could be enriched by asymptotic giant branch (AGB) stars with masses around $3 - 5 M_{\odot}$.

Keywords: stars: chemically peculiar – stars: abundances – stars: evolution

1. INTRODUCTION

Globular clusters (GCs) were traditionally considered as simple stellar population systems, i.e., all member stars originate from the same molecular cloud, share the same age and abundances. However, an increasing number of studies (see e.g. Gratton et al. 2012; Piotto et al. 2015; Milone et al. 2017; Tang et al. 2017, 2018, and references therein) show that almost all GCs host two or more groups of stars with different chemical abundances, which is so-called multiple populations (MPs). Stars with enhanced N, Na, (sometimes He, Al, and Si), but depleted C, O, (sometimes Mg), are traditionally called

“second generation” (SG) stars (or “second population” stars), distinct from the primordial “first generation” (FG) stars. SG stars and FG stars possibly differ in age by a few hundred Myr (e.g., Conroy 2012; Bekki et al. 2017) but have the same $[\text{Fe}/\text{H}]$ abundance (e.g., Carretta et al. 2010b). Furthermore, SG stars have different radial distribution as FG stars in most GCs, generally being more centrally concentrated (e.g. Lardo et al. 2011; Simioni et al. 2016), although a few exceptions has also been reported: some GCs show that FG stars concentrated more in the inner region (e.g. Larsen et al. 2015; Vanderbeke et al. 2015; Lim et al. 2016), while some GCs show similar spatial distribution between these two populations (e.g. Dalessandro et al. 2014; Miholics et al. 2015).

Most scenarios trying to explain the MP phenomenon assume that chemically enriched SG stars were formed in light-element-polluted environment formed partially from the ejecta of FG stars. These stars are generally

Corresponding author: Baitian Tang
tangbt@mail.sysu.edu.cn

^{a)} We refer Milky Way field stars as Milky Way halo field stars unless specified in this paper.

enriched in light elements, such as C, N, Na, etc, which are also known as enriched populations. The proposed astrophysical sites include very massive stars (VMSs), fast rotating massive stars (FRMSs), asymptotic giant branch (AGB) stars, etc, although none is currently able to explain all observational constraints (e.g., Bastian & Lardo 2018).

On one hand, stellar evolution of massive stars leads to the mass loss of GCs, especially for FG stars (e.g., D’Ercole *et al.* 2008; Schaerer & Charbonnel 2011). On the other hand, dynamical evolution, including internal two-body interaction and external tidal stripping, also contribute to the stellar loss of GCs (Lamers *et al.* 2010). FG stars are chemically similar to normal field stars, while SG stars show peculiar abundances in several light elements. Thus, identifying field stars with similar chemical pattern as GC SG stars could potentially add important observational constraints to help motivate theoretical scenarios.

With the help of large spectroscopic surveys, the search for these chemically peculiar stars is becoming more efficient. N is usually enhanced in GC SG stars, and relatively easier to measure in low-resolution spectroscopic survey, therefore, N-rich field stars found in early surveys are usually linked to stars escaped from GCs (e.g., Martell & Grebel 2010; Martell *et al.* 2011; Koch *et al.* 2019). Recently, high resolution spectroscopic surveys, like the Apache Point Observatory Galactic Evolution Experiment (APOGEE; Majewski *et al.* 2017) have led to the discovery of a large group of N-rich field stars (Fernández-Trincado *et al.* 2016, 2017, 2019; Martell *et al.* 2016; Schiavon *et al.* 2017). In this respect, the unprecedented large number (more than 10^6) of low-resolution stellar spectra available in the Large Sky Area Multi-Object Fiber Spectroscopic Telescope (LAMOST) survey (Zhao *et al.* 2012) greatly increase the efficiency and accuracy of such a search. Tang *et al.* (2019) (hereafter Paper I) and Tang *et al.* (2020) (hereafter Paper II) have identified ~ 100 N-rich stars from a sample of metal-poor, red giant branch (RGB) field stars based on CN3839, CN4142, and CH4300 spectral indices using LAMOST DR3 (data release) and DR5. These N-rich field stars show similar kinematics as Galactic GCs, which are a mixture of GCs formed in situ and ex situ (e.g., Massari *et al.* 2019). To further explore the connection between N-rich field stars and GCs using the idea of “chemical tagging”, we investigate in optical high resolution spectra to carefully examine more than 20 elements in this work. Several elements that we shown in this work (e.g., Na, Ba, Eu) are important for constraining the nature of MPs, but rarely available in near-infrared studies.

The paper is organized as follows. In Section 2, we describe our data and reduction processes. We carefully compare our derived abundances with literature values of Milky Way (MW) GCs, MW (disc and halo stars) and dwarf galaxies to investigate the origin of N-rich field stars in Section 3 and 4. Our final conclusion is given in Section 5.

2. THE DATA

2.1. Follow-up observations and data reduction

We started the selection of observable targets from our LAMOST N-rich field star sample (Paper I and Paper II), which are mostly located in the northern sky. Fifteen stars with $\text{DEC} < 10^\circ$ and a reasonable airmass were selected. Our follow-up observations were taken using the MIKE (Magellan Inamori Kyocera Echelle, Bernstein *et al.* 2003) spectrograph on the Magellan Clay telescope (Shectman & Johns 2003) at Las Campanas Observatory, Chile. The data were taken in two runs, 2019/07 and 2020/02. The blue and red detectors were used simultaneously to cover $3200 < \lambda < 5000 \text{ \AA}$ (blue side) and $4900 < \lambda < 10000 \text{ \AA}$ (red side). We used the 0.7” slit and 2x2 spatial on-chip binning to achieve nominal spectral resolution of 35k/28k on the blue side and red side, respectively. Depending on the observation schedule and the brightness of the star, we took several exposures to ensure SNR (signal-to-noise ratio) > 50 over most wavelength of the red detector (Table 1).

We reduced the observational data using the *CarPy* package (Kelson *et al.* 2000; Kelson 2003). The observed spectral images were bias-subtracted, flat-field corrected, wavelength calibrated, scatter-light and sky subtracted. The multi-order reduced spectra were then merged into a single spectrum.

2.2. Stellar parameters and chemical abundances

Stellar parameters and chemical abundances were analyzed using Brussels Automatic Stellar Parameter (BACCHUS) code (Masseron *et al.* 2016). We briefly describe the basic procedures here, readers are referred to Masseron *et al.* (2016) for detailed descriptions.

The equivalent widths (EW) of Fe I and Fe II absorption lines are first measured. To derive stellar parameters, several stellar parameters are attempted before they converge: T_{eff} is determined by obtaining null trend for the abundance of iron lines against excitation potential (see Figure 11 in Appendix); $\log g$ is obtained by ionisation equilibrium between Fe I and Fe II lines; metallicity is obtained by the mean of individual line abundances relative to the solar value; microturbulence velocity is determined by obtaining null trend for the abundance of iron lines against equivalent widths. For

initial guess, we used photometric T_{eff} calculated from 2MASS photometry (González Hernández & Bonifacio 2009) and $\log g$, $[\text{Fe}/\text{H}]$ from LAMOST suggested values. Our derived stellar parameters using BACCHUS are shown in Table 1. Note that most of our stars show $\log g$ greater than 2. Because the red clump feature is located at $\log g \sim 2$ (Paper II), our sample stars are mostly RGB stars.

To derive chemical abundance for a given absorption line, a sigma-clipping is first applied on the selected continuum points around the targeted line, then a linear fit is used for the remaining points as the continuum. Therefore, the code can detect significantly bad fits, like a sudden drop in the spectrum due to bad pixels in the detectors. Observed spectra and model spectra are compared in four different methods to determine abundances: χ^2 minimization, line intensity, equivalent width, and spectral synthesis (see Figure 12 in Appendix). Furthermore, the code gives each of them a flag to indicate the estimation quality. When multiple transition lines are detected for a given element, the lines that satisfy the followings are chosen: 1) $\lambda > 5000 \text{ \AA}$ (for better SNR, see Figure 10 in Appendix); 2) all four determination methods are flagged as good (= 1); 3) $\text{SNR} > 40$. Then, the mean value of the chemical abundances of different absorption lines from χ^2 minimization is given as the estimated abundance for the given element. If no line meets the above criteria, the abundance is not estimated. The derived chemical abundances of our targets are given in Table 2.

In this work, we analyzed the internal errors by propagating the typical errors in T_{eff} , $\log g$, $[\text{Fe}/\text{H}]$. The typical errors are set as $\Delta T_{\text{eff}} = 50 \text{ K}$, $\Delta \log g = 0.1 \text{ dex}$, $\Delta [\text{Fe}/\text{H}] = 0.05 \text{ dex}$. The total estimated error is thus calculated as: $\sigma_{\text{tot}} = ((\sigma_{\Delta T_{\text{eff}}})^2 + (\sigma_{\Delta \log g})^2 + (\sigma_{\Delta [\text{Fe}/\text{H}]})^2)^{1/2}$. The abundance errors of a typical star (star #88 from Paper II) are shown in Table 3 as an example.

3. RESULTS

3.1. Na-O relation

The anti-correlation between Na and O is observed in almost all GCs (Carretta et al. 2009b, 2010b; Gratton et al. 2012), which is arguably the most characteristic MP property of GC member stars. The Na-O anti-correlation is suggested to originate from the CNO cycle and the NeNa cycle activated during lower temperature H-burning. If our N-rich field stars show compatible Na and O abundances as the GC enriched populations, it would be a supportive evidence for their GC origin scenario. For the reference of chemical abundances of GC stars, we used the observed data of 19 GCs from

Carretta et al. (2009b). Based on the Na and O abundances, they separated members of each GC into three components, P (primordial) component, I (intermediate) component, and E (extreme) component. FG stars (or P component) are assumed to have similar O and Na abundances as field stars of the same metallicity, while I and E components are all considered to be SG stars.

Following the convention to measure O abundances (e.g. Carretta et al. 2009b), we only used $[\text{O I}] \lambda\lambda 6300, 6363 \text{ \AA}$ forbidden lines to minimize the effect of non-local thermodynamic equilibrium (NLTE) correction. If no measurable line is found, the mean value from χ^2 minimization is given as the upper limit. The Na and O abundances are shown in Figure 1, where GC stars from Carretta et al. (2009b) are shown as background dots and contours. In order to match the metallicities between our N-rich field stars and GCs, only GCs with $-1.8 \leq [\text{Fe}/\text{H}] \leq -1.0$ are used. Though a clear anti-correlation between Na and O with large spread is found for GC stars, the separation between FG and SG stars is not clear-cut. Seven stars have measurable O abundances. Most N-rich field stars basically show consistent Na and O abundances with those in GCs, except for two stars: one with $[\text{O}/\text{Fe}] \sim 1$ and the other with $[\text{Na}/\text{Fe}] \sim 1$. Based on their measurable Na abundances, most N-rich field stars are located in the transition region between FG and SG stars, thus it is difficult to verify their SG origin.

3.2. Mg-Al relation

Mg-Al anti-correlation is another common feature found in low metallicity GCs ($[\text{Fe}/\text{H}] < -1.0$, Pancino et al. 2017), which is suggested to be the consequence of Mg-Al cycle activated at higher core temperature during H-burning (Arnould et al. 1999). Our N-rich field stars are shown as red symbols in Figure 2. We note that the red pentagons are chemical abundances derived in Paper II using APOGEE spectra. In the background, GC stars from Carretta et al. (2009a) are separated into FG (orange) and SG (blue) stars as previously mentioned.

Though GC FG and SG stars are wide-spread and even overlap in $[\text{Al}/\text{Fe}]$ distribution, FG stars seldomly exceed $[\text{Al}/\text{Fe}] \sim 0.5$ (excluding upper limits). On the other hand, GC SG stars may show low $[\text{Al}/\text{Fe}]$ down to 0, and thus a lower $[\text{Al}/\text{Fe}]$ cannot exclude the possibility that the star belongs to SG. In this sense, almost half of our N-rich field star sample show $[\text{Al}/\text{Fe}] > 0.5$, which are probable SG stars. Those stars with $[\text{Al}/\text{Fe}] > 0.5$ also have compatible $[\text{Mg}/\text{Fe}]$ to ensure that they are covered by the Mg-Al anti-correlation of GC Al-enhanced stars. There are two extremely Mg depleted N-rich field stars ($[\text{Mg}/\text{Fe}] < -0.4$), but one of them has

Table 1. Stellar parameters

Id	RA	DEC	T_{eff} (K)	$\log g$ (dex)	[Fe/H] (dex)	G_{mag} (mag)	microturbulence (km s^{-1})	RV (km s^{-1})	airmass	exposure time (s)
9 (II)	58.221019	7.203154	4312	0.65	-1.34	13.63	1.78	69.0	1.42	4800
38 (II)	258.215699	8.130489	4604	0.73	-1.62	12.57	2.04	-146.0	1.90	3600
47 (II)	214.054033	-2.145359	4953	2.14	-1.38	12.06	1.95	66.5	1.80	3600
58 (II)	197.656039	-6.979531	5213	2.84	-1.45	14.45	1.78	-27.0	1.10	5400
62 (II)	122.120480	1.946907	5020	2.36	-1.42	12.87	1.56	147.0	1.17	5400
65 (II)	233.551930	0.326274	4806	1.69	-1.63	12.76	1.45	-72.5	1.57	3600
67 (I)	317.852325	-2.385546	5265	2.12	-0.97	13.06	2.46	-5.0	1.14	3600
69 (I)	150.981537	1.298311	5129	3.02	-1.07	12.22	1.26	50.0	1.12	3600
80 (I)	134.988876	1.055260	4800	1.37	-1.88	13.79	1.35	179.0	1.00	5400
82 (I)	195.094070	-7.636771	5017	1.90	-1.06	12.59	1.60	-6.0	1.50	5400
86 (I)	239.791901	10.020472	5149	2.91	-0.98	14.10	1.37	-141.0	1.47	3600
88 (I)	244.844238	9.523706	4879	2.31	-1.02	13.16	1.51	-127.0	1.88	3600
94 (I)	166.054535	8.444023	5161	2.88	-1.18	14.44	1.33	51.0	2.00	3600
97 (I)	222.293640	10.045577	4762	2.20	-1.25	13.12	1.34	-31.0	1.49	3600
98 (I)	199.145416	10.957638	4529	0.77	-1.07	10.59	2.03	84.0	1.30	3600

The *Id* is the corresponding id in [Paper II](#) (table 3), with (I) and (II) indicate that they are from [Paper I](#) and [Paper II](#), respectively.

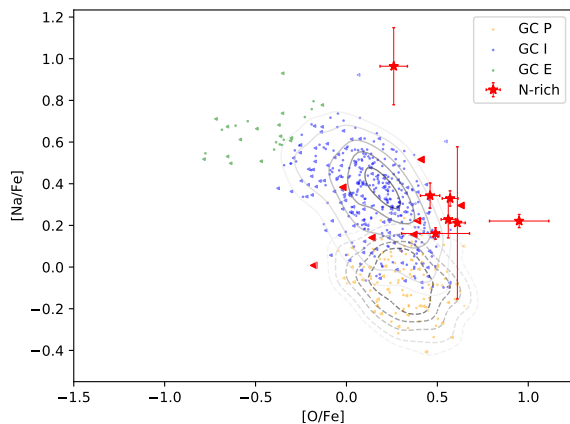


Figure 1. $[\text{Na}/\text{Fe}]-[\text{O}/\text{Fe}]$ relation. Na and O abundances of N-rich field stars are shown as red symbols. Upper limits in O abundances are shown as triangles, while detections are shown as stars with error bars. The Na and O abundances of the individual stars in the GCs from [Carretta et al. \(2009b\)](#) are over plotted for comparison. Green symbols indicate the GC E component. Blue symbols indicate the GC I component, while orange symbols indicate the GC P component. Upper limits in O abundances are shown as triangles, while detections are shown as dots. The solid and dashed contours indicate the number densities of I component and P component, respectively.

been reported in [Paper II](#) and [Fernández-Trincado et al. \(2019\)](#). The Mg depleted N-rich field stars were also discussed in [Fernández-Trincado et al. \(2016, 2017\)](#). The Mg depletion in N-rich field stars is rare, it would be interesting to know if these Mg-depleted N-rich field stars have gone through additional nucleosynthesis. Mean-

while, the other half of N-rich field stars ($[\text{Al}/\text{Fe}] < 0.5$) show Mg and Al abundances consistent with GC FG/SG stars. Though chemically being less distinguishable from FG stars based on their Mg and Al abundances, we cannot rule out the possibilities that lower $[\text{Al}/\text{Fe}]$ N-rich field stars are SG stars, as more metal-rich GCs tend to show similar Al abundances for FG and SG stars ([Pancino et al. 2017](#)). Furthermore, using APOGEE GC stars ([Mészáros et al. 2020](#)), we found that lower Al abundances ($[\text{Al}/\text{Fe}] < 0.5$) N-rich field stars tend to be more metal-rich in the sample (Figure 3), tentatively agree with the aforementioned GC behavior.

3.3. α -elements

The α -elements are mainly generated in massive stars through type II supernovae (SNe II), consequently their recycle timescale in the interstellar medium is much smaller than that of iron, which is mainly produced in type Ia supernovae (SNe Ia). As a result, the $[\alpha/\text{Fe}]$ abundance is initially enhanced, and starts to decline with $[\text{Fe}/\text{H}]$ after SN Ia explosion rate reaches a maximum ([Matteucci & Greggio 1986](#)). The decline point, or the knee in $[\alpha/\text{Fe}]$ vs. $[\text{Fe}/\text{H}]$ trend, is related to star formation rate and thus galaxy mass: the less massive the galaxy is, the more metal-poor is the $[\alpha/\text{Fe}]$ turnover. O and Mg are commonly classified as hydrostatic α -elements, while Si, Ca, and Ti are classified as explosive α -elements ([Woosley & Weaver 1995](#)), implying different nucleosynthetic processes.

The $[\text{Mg}/\text{Fe}]-[\text{Fe}/\text{H}]$ relation is shown in the upper left panel of Figure 4. In the background, we also include MW halo and disc stars, dwarf galaxy (Sculptor and Sagittarius) stars, and APOGEE GC stars

Table 2. Chemical abundances

Element	9 (II)	38 (II)	47 (II)	58 (II)	62 (II)	65 (II)	67 (I)	69 (I)
[O/Fe]	< 0.14	< -0.02	0.57	< 0.41	< -0.18	< 0.16	0.49	< 0.37
[Na/Fe]	0.14	0.38	0.33	0.52	0.01	...	0.16	0.16
[Mg/Fe]	0.19	0.31	0.45	0.31	-0.38	0.31	0.41	0.41
[Al/Fe]	0.21	1.29	0.28	0.39	0.68	0.83	0.26	...
[Si/Fe]	0.11	0.51	0.14	0.30	0.45	0.45	0.41	0.35
[S/Fe]	...	0.55	...	0.59	0.20	0.52
[Ca/Fe]	0.11	0.44	0.27	0.33	0.38	0.39	0.10	0.41
[Sc/Fe]	-0.23	0.09	0.19	0.15	0.34	-0.04	-0.17	0.41
[Ti/Fe]	-0.02	0.21	0.41	0.31	0.17	0.35	0.22	0.34
[V/Fe]	-0.22	0.05	0.22	0.23	-0.09	0.10	0.10	0.03
[Cr/Fe]	-0.12	-0.15	-0.06	-0.14	-0.24	...	-0.28	-0.03
[Mn/Fe]	-0.60	-0.36	-0.37	-0.39	-0.60	-0.63	-0.36	-0.50
[Co/Fe]	-0.26	-0.02	0.08	0.10	-0.01	...	0.13	-0.05
[Ni/Fe]	-0.29	-0.02	0.02	0.04	-0.14	-0.07	0.13	-0.01
[Y/Fe]	-0.08	-0.09	-0.05	-0.04	-0.01	0.04	-0.10	0.22
[Zr/Fe]	-0.00	0.22	0.42	...	0.35	...	0.31	...
[Ba/Fe]	-0.17	-0.20	-0.02	0.22	0.23	0.89	0.28	0.38
[La/Fe]	0.07	0.08	0.30	0.33	0.31	0.71	0.26	0.38
[Ce/Fe]	-0.09	-0.05	0.15	0.35	0.24	...	0.12	0.20
[Nd/Fe]	0.18	0.18	0.39	0.76	0.37	...	0.28	...
[Eu/Fe]	0.41	0.29	0.65	0.55	0.53	...	0.28	0.27
Element	80 (I)	82 (I)	86 (I)	88 (I)	94 (I)	97 (I)	98 (I)	
[O/Fe]	0.26	0.46	0.95	0.56	< 0.39	< 0.63	0.61	
[Na/Fe]	0.96	0.34	0.22	0.23	0.22	0.30	0.21	
[Mg/Fe]	0.72	0.51	0.19	0.27	0.54	0.24	0.48	
[Al/Fe]	0.74	0.20	0.21	0.14	0.74	1.01	...	
[Si/Fe]	0.48	0.55	0.16	0.26	0.42	0.54	0.43	
[S/Fe]	0.82	0.27	0.59	
[Ca/Fe]	0.63	0.41	0.32	0.23	0.54	0.60	0.16	
[Sc/Fe]	0.10	0.08	0.30	0.20	...	0.14	-0.39	
[Ti/Fe]	0.36	0.25	0.36	0.22	0.43	0.50	0.04	
[V/Fe]	0.16	0.07	0.11	-0.05	0.20	0.19	-0.22	
[Cr/Fe]	-0.02	-0.03	0.08	-0.16	0.10	0.18	-0.15	
[Mn/Fe]	-0.39	-0.37	-0.38	-0.51	-0.32	-0.32	-0.49	
[Co/Fe]	0.04	0.01	0.10	-0.17	0.05	0.06	-0.01	
[Ni/Fe]	0.15	0.03	0.04	-0.09	0.08	0.21	-0.01	
[Y/Fe]	-0.06	0.16	0.16	0.08	0.17	0.33	...	
[Zr/Fe]	0.34	0.43	0.67	...	
[Ba/Fe]	0.31	...	0.44	0.46	0.40	0.76	...	
[La/Fe]	0.21	0.45	0.74	0.63	0.42	0.46	-0.12	
[Ce/Fe]	0.16	0.33	0.29	0.32	0.22	...	-0.14	
[Nd/Fe]	0.29	0.35	0.82	0.49	0.51	0.48	0.02	
[Eu/Fe]	...	0.50	0.90	...	0.38	

(violin shaped symbols).¹ Each violin shaped symbol corresponds to one GC. The center value and min-max values are determined by its GC members selected from the APOGEE survey (e.g. [Mészáros et al. 2020](#); [Fernández-Trincado et al. 2020](#)). [Mg/Fe] of our N-rich field stars are inside the min-max range of APOGEE

GCs of similar metallicity, which does not contradict with the hypothesis that N-rich field stars come from GCs. However, in situ GCs (GCs that identified as main disc or main bulge) and accreted GCs are largely overlapped especially in our chosen metallicity range ($-1.8 < [\text{Fe}/\text{H}] < -1.0$), which prevents us distinguishing their in situ or accreted GC origin. Meanwhile, our N-rich field stars are mostly covered by both data points of MW stars and dwarf galaxies, indicating a mixture of in situ stars and extragalactic stars. This is consistent with their kinematics in [Paper II](#).

¹ There are 31 GCs compiled by [Mészáros et al. \(2020\)](#) in total. In our Figure 3 and 4, we do not show Omega cen due to its large metallicity spread. Four GCs, which have metallicities smaller than -2.0, are not shown, neither. Among the rest 26 GCs, there are eight in situ GCs colored with yellow green and 18 accreted GCs colored with sky blue.

Table 3. Errors of chemical abundances propagated from atmospheric parameters for star #88.

Element	abundance	$\Delta T_{\text{eff}} = 50$ (K)	$\Delta \log(g) = 0.1$ (dex)	$\Delta[\text{Fe}/\text{H}] = 0.05$ (dex)	σ_{tot}
$\Delta([\text{O}/\text{Fe}])$	0.56	0.00	0.03	0.03	0.04
$\Delta([\text{Na}/\text{Fe}])$	0.23	0.03	0.00	0.08	0.09
$\Delta([\text{Mg}/\text{Fe}])$	0.27	0.03	0.00	0.00	0.03
$\Delta([\text{Al}/\text{Fe}])$	0.14	0.02	0.00	0.02	0.03
$\Delta([\text{Si}/\text{Fe}])$	0.26	0.01	0.01	0.02	0.03
$\Delta([\text{S}/\text{Fe}])$
$\Delta([\text{Ca}/\text{Fe}])$	0.23	0.04	0.00	0.00	0.04
$\Delta([\text{Sc}/\text{Fe}])$	0.20	0.00	0.03	0.02	0.04
$\Delta([\text{Ti}/\text{Fe}])$	0.22	0.04	0.01	0.01	0.04
$\Delta([\text{V}/\text{Fe}])$	-0.05	0.07	0.00	0.00	0.07
$\Delta([\text{Cr}/\text{Fe}])$	-0.16	0.03	0.02	0.04	0.06
$\Delta([\text{Mn}/\text{Fe}])$	-0.51	0.08	0.01	0.01	0.08
$\Delta([\text{Co}/\text{Fe}])$	-0.17	0.06	0.01	0.01	0.07
$\Delta([\text{Ni}/\text{Fe}])$	-0.09	0.03	0.01	0.03	0.04
$\Delta([\text{Y}/\text{Fe}])$	0.08	0.04	0.04	0.05	0.07
$\Delta([\text{Zr}/\text{Fe}])$
$\Delta([\text{Ba}/\text{Fe}])$	0.46	0.01	0.05	0.06	0.08
$\Delta([\text{La}/\text{Fe}])$	0.63	0.01	0.04	0.01	0.05
$\Delta([\text{Ce}/\text{Fe}])$	0.32	0.01	0.02	0.03	0.04
$\Delta([\text{Nd}/\text{Fe}])$	0.49	0.03	0.04	0.07	0.09
$\Delta([\text{Eu}/\text{Fe}])$

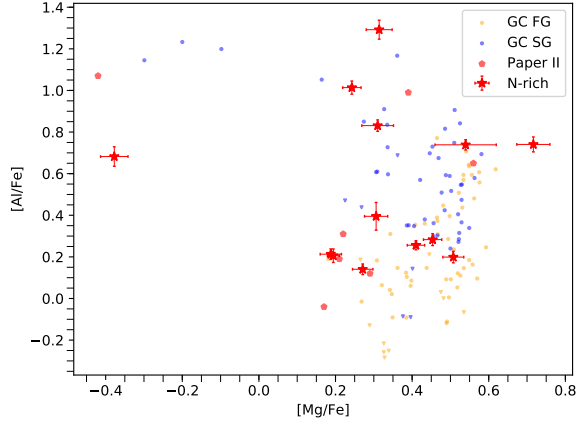


Figure 2. $[\text{Mg}/\text{Fe}]$ - $[\text{Al}/\text{Fe}]$ relation. Mg and Al abundances of N-rich field stars are shown as red symbols: 15 N-rich stars observed with MIKE spectra are marked as red stars with error bars, while seven N-rich stars with APOGEE spectra (Paper II) are marked as red pentagons. Orange and blue symbols correspond to GC first generation (P component) and second generation (I and E component) stars, respectively (Carretta *et al.* 2009a). Upper limits in Al abundances of GC stars are shown as triangles, while detections are shown as small dots.

As the atomic number increases, Si, Ca, and Ti become more stable against H-burning. Si abundance is suggested to vary by the “Si-leakage” during Mg-Al cycle when the core temperature reaches as high as $T \sim 65 \times 10^6$ K (Carretta *et al.* 2009a). Most GCs do

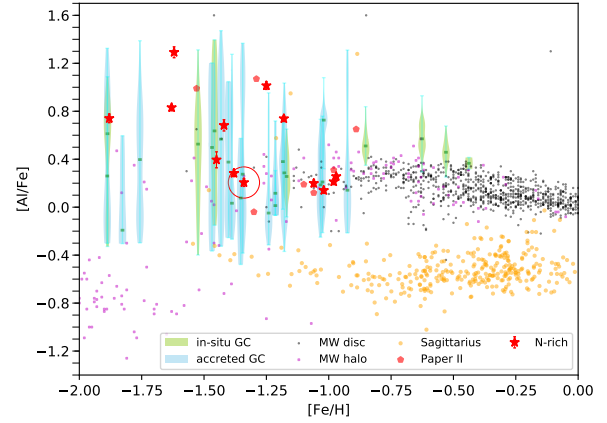


Figure 3. $[\text{Al}/\text{Fe}]$ - $[\text{Fe}/\text{H}]$ relation. Al abundances of N-rich sample with MIKE spectra are shown as red symbols (same meanings as mentioned in Figure 2). Magenta squares correspond to MW stars from halo (92 out of 168 stars from Fulbright 2000, 35 stars from Cayrel *et al.* 2004, 234 out of 253 stars from Barklem *et al.* 2005, 131 out of 199 stars from Yong *et al.* 2013, 287 out of 313 stars from Roederer *et al.* 2014), while black dots for MW stars from disc (174 out of 181 stars from Reddy *et al.* 2003, 153 out of 176 stars from Reddy *et al.* 2006, 679 out of 714 stars from Bensby *et al.* 2014). Orange circles correspond to Sagittarius (Hasselquist *et al.* 2017; Hayes *et al.* 2020). Violin shaped symbols indicate GC stars from APOGEE (Mészáros *et al.* 2020). In situ GCs are colored with yellow green, while accreted GCs are colored with sky blue. Star #9 with high extragalactic GC origin possibility are labeled with large red circle.

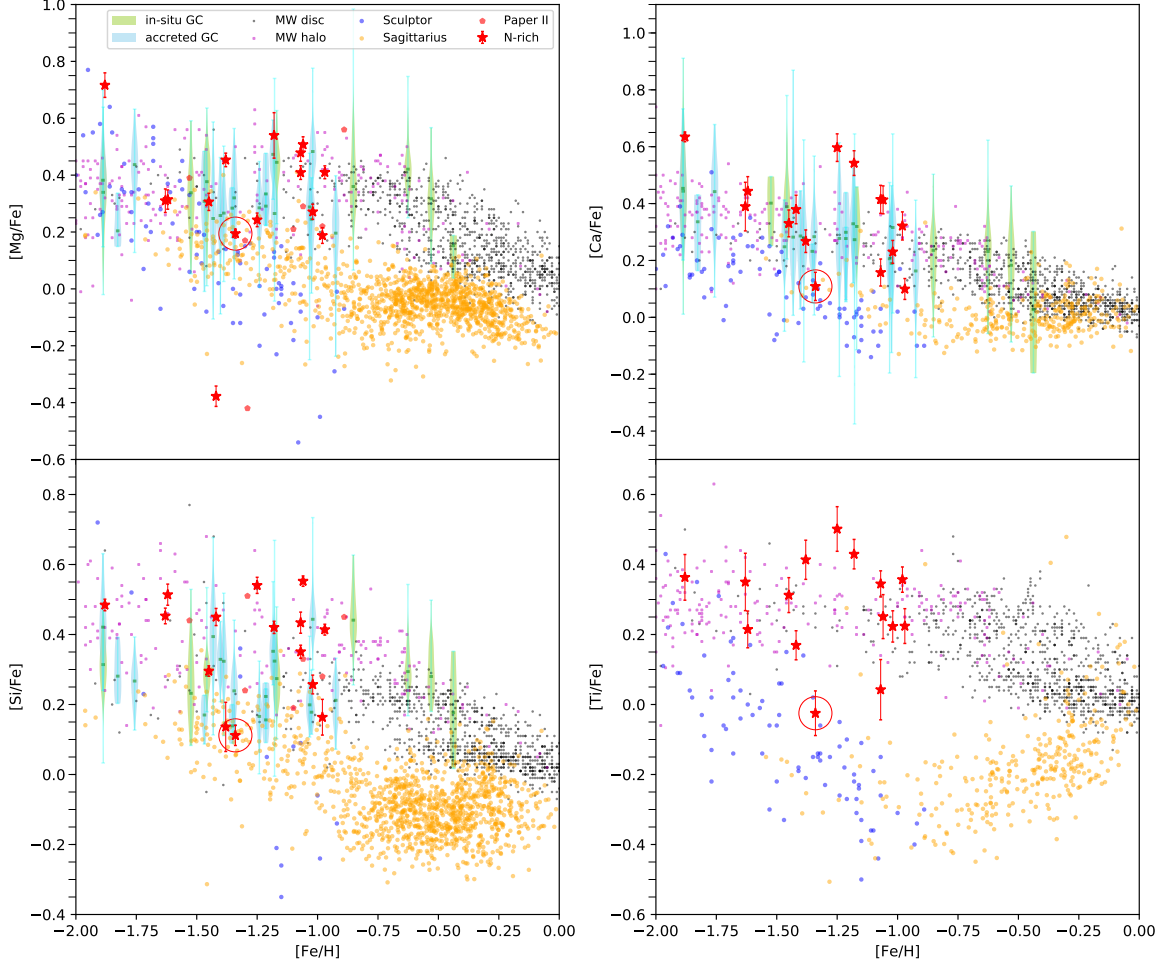


Figure 4. $[\text{Mg}/\text{Fe}]$ - $[\text{Fe}/\text{H}]$ (upper left), $[\text{Si}/\text{Fe}]$ - $[\text{Fe}/\text{H}]$ (bottom left), $[\text{Ca}/\text{Fe}]$ - $[\text{Fe}/\text{H}]$ (upper right), and $[\text{Ti}/\text{Fe}]$ - $[\text{Fe}/\text{H}]$ (bottom right) relation. Symbols are same as Figure 3. Blue circles represent stars from Sculptor (Hill et al. 2019).

not show significant variation in Ca (e.g., Carretta et al. 2010a), except for several massive GCs with possible iron spread (Carretta & Bragaglia 2020). No significant Ti variation among GC members is reported to the best of our knowledge.

Interestingly, Horta et al. (2020) reported that in situ GCs may have higher $[\text{Si}/\text{Fe}]$ compared to accreted GCs for $[\text{Fe}/\text{H}] > -1.5$. The $[\text{Si}/\text{Fe}]$ difference between two groups of GCs become less distinguishable as metallicity decreases. The background MW stars, dwarf galaxy stars (Sculptor and Sagittarius) of Figure 4 (bottom left panel) support similar statement of Horta et al. (2020) for field stars, though the threshold metallicity can be only vaguely located at $-1.5 < [\text{Fe}/\text{H}] < -1.0$. Upper right panel and bottom right panel of Figure 4 shows the Ca and Ti abundances distributions of our N-rich field stars, along with background MW stars, dwarf galaxy stars and GC star distribution (violin shaped symbols), respectively. Jönsson et al. (2020) warned against using

APOGEE-derived Ti abundances, since the Ti I and Ti II abundances from APOGEE pipeline may have unknown defects or large scatters, so $[\text{Ti}/\text{Fe}]$ for APOGEE GCs are not shown in this work.

Looking at Mg, Si, Ca, Ti abundances versus $[\text{Fe}/\text{H}]$ simultaneously, interesting results emerge: (1) The α -element difference between in situ (MW) stars and accreted (dwarf galaxy) stars is most significant for Ti, compared to Mg, Si and Ca. It is promising to use $[\text{Ti}/\text{Fe}]$ for future works to distinguish accreted stars. (2) The $[\alpha/\text{Fe}]$ from APOGEE survey (violin shaped symbols) cover most of the N-rich field stars, again supporting their GC origin. (3) Seven metal-rich ($-1.25 \leq [\text{Fe}/\text{H}] \leq -0.95$) N-rich field stars show abundances more consistent with MW stars, indicating a higher possibility of in situ origin. (4) At the lower end of the $[\alpha/\text{Fe}]$ distribution, star #9 (labeled with large red circle in Figure 4) shows consistently low Mg, Si, Ca, and Ti abundances similar to stars in dwarf galaxies, although

it shows similar [Al/Fe] as MW disc and halo stars (Figure 3). However, Al can be enhanced in GCs without altering much of its α -abundances. Is it possible that this star has an extragalactic GC origin? We will further discuss this with more chemical information below.

3.4. Iron-peak elements

Though Type Ia SNe, runaway deflagration obliterations of white dwarfs, have a signature more tilted towards the iron-peak group (Nomoto *et al.* 1997), the solar composition of the iron-peak elements are in fact a heterogeneous combination of both Type Ia SNe and core collapse Type II SNe (Woosley & Weaver 1995). As dwarf galaxies and MW have different star formation timescale, this discrepancy may manifest itself in iron-peak elements. Figure 5 show that MW stars (black dots and magenta squares) and dwarf galaxy stars (blue circles) have appreciable different distributions in [Sc/Fe], [V/Fe], and [Co/Fe] vs. [Fe/H] graphs over the given metallicity range, especially in metal-rich part ([Fe/H] ≥ -1.25). For these three elements, more metal-rich N-rich field stars ($-1.25 \leq [\text{Fe}/\text{H}] \leq -0.95$) show distributions more similar to MW stars, confirming a higher possibility of in situ origin (Section 3.3). For [Cr/Fe], [Mn/Fe] and [Ni/Fe], MW stars and dwarf galaxy stars show less distinguishable difference. The discrepancies in iron-peak element of MW stars and dwarf galaxies are not evident in metal-poor part (especially for $-1.25 < [\text{Fe}/\text{H}] < -1.5$) due to lack of data. However, if a linear relation of iron-peak abundances and metallicity is assumed for both MW (halo and disc) and dwarf galaxies, the dwarf galaxies would have lower iron-peak abundances. Therefore, star #9 with low α -element abundances also show lower abundances in [Sc/Fe], [V/Fe], [Co/Fe], agree with dwarf galaxies, which supports its possible extragalactic GC origin.

3.5. Neutron capture elements

Elements heavier than iron are generated via neutron-capture processes. Depending on the relative speed of neutron capture compared to β -decay, the neutron-capture processes are divided into rapid (r -) and slow (s -) ones. The main s -process elements are synthesized by AGB stars during thermal pulsations (Busso *et al.* 2001; Karakas & Lattanzio 2014). The astrophysical sites of producing r -process elements have been debated over the past sixty years (e.g., Thielemann *et al.* 2011; Kajino *et al.* 2019). The more popular models includes core collapse SNe (e.g., Woosley *et al.* 1994) and neutron star mergers (e.g., Côté *et al.* 2018; Watson *et al.* 2019).

Y, Zr, Ba, La, Ce, Nd and Eu are neutron-capture elements detectable in most of our sample stars across

the observed wavelength. According to the recent work of Kobayashi *et al.* (2020), Y, Zr, Ba, La, Ce and Nd are mostly produced through s -process in the current Universe, while Eu is produced through r -process. The neutron capture element abundances of our N-rich field stars are compared with MW stars in Figure 6. We see that the scatter of abundances in MW stars increases as metallicity decreases, given that feature lines are weaker in more metal-poor stars. Generally, we see consistency between our N-rich field stars and MW stars, but several stars with enhanced [Ba/Fe], [La/Fe] and [Eu/Fe] are also noticed.

Two nuclear reactions are the major neutron excess sources in AGB stars: $^{13}\text{C}(\alpha, n)^{16}\text{O}$ and $^{22}\text{Ne}(\alpha, n)^{25}\text{Mg}$. The first reaction dominates the low mass AGB stars, while the latter one is mainly found in massive AGB stars (Cristallo *et al.* 2015). As the number of free neutrons per iron seed increases, the s -process flow first seeds the light s -process peak (Sr–Y–Zr), extending to ^{136}Ba , and then reaches the heavy s -process peak (Ba–La–Ce–Pr–Nd), extending to ^{204}Pb – ^{207}Pb (Bisterzo *et al.* 2014). Therefore, the heavy s -process element to light s -process element ratio ([hs/ls]) is closely related to metallicity and initial stellar mass. In this work, [hs/ls] is defined as [hs/Fe] – [ls/Fe], where [hs/Fe] = ([Ba/Fe] + [La/Fe] + [Nd/Fe])/3, and [ls/Fe] = ([Y/Fe] + [Zr/Fe])/2. In our sample, there are six stars with all five s -process elements (Figure 7). Five stars show consistent [hs/ls] values as other MW stars in the same metallicity range. The grid lines of Cristallo *et al.* (2015) indicate these stars are enriched by AGB stars of masses around 3 – 5 M_{\odot} .

The ratio between s -process element and r -process element is an indicator of the neutron-capture speed compared to β -decay, which could be related to the contribution of AGB stars (thus SNe Ia) over SNe II and neutron star mergers. Ba is commonly used to represent the heavy s -process elements, while Y for the light s -process elements. A gradual rise in [Y/Eu] and [Ba/Eu] with increasing metallicity is seen in Figure 8, which was addressed in e.g., McWilliam (1998). The upper panel of Figure 8 shows that MW field stars, MW GC stars and dwarf galaxy stars overlap in the [Ba/Eu]-[Fe/H] space; In the lower panel, [Y/Eu] of dwarf galaxies from Shetrone *et al.* (2003) and Venn *et al.* (2012) are slightly smaller compared to MW field stars and MW GC stars at similar metallicity range, but with substantial overlap (also see Figure 19 of Venn *et al.* 2012). Though most N-rich field stars show consistent abundances with other studies, we are not able to distinguish their in situ or extragalactic origin here. Bisterzo *et al.* (2014) suggested that [Ba/Eu] ~ -0.7 is the typical value for a

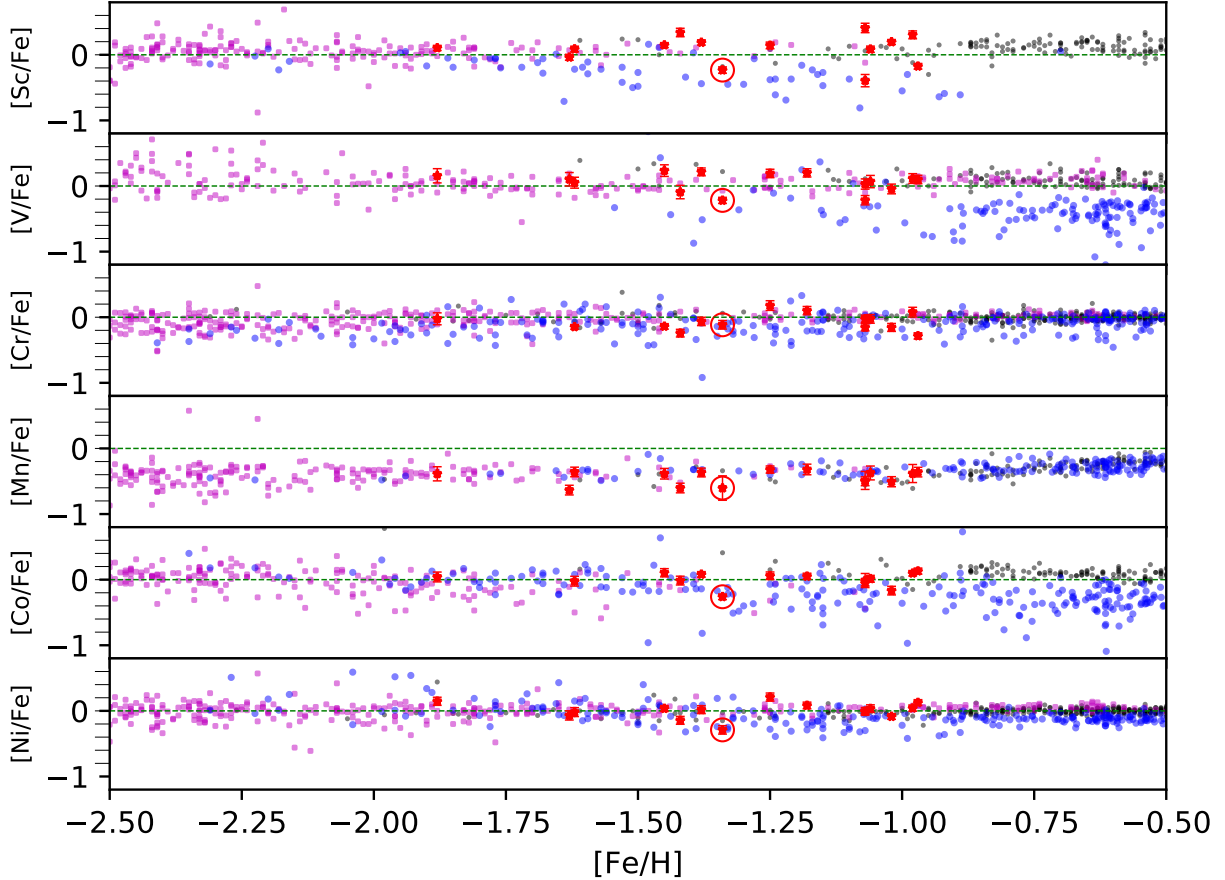


Figure 5. Abundances of iron peak elements vs. $[\text{Fe}/\text{H}]$. Abundances of N-rich stars are shown as red stars, while magenta squares and black dots correspond to MW stars from halo and disc, respectively (same sources as in Figure 3). Blue circles correspond to stars from dwarf galaxies (Sagittarius, Sculptor, Fornax, Carina, Leo I, [Hasselquist et al. 2017](#); [Hill et al. 2019](#); [Shetrone et al. 2003](#)).

pure r -process. Most N-rich field stars show $[\text{Ba}/\text{Eu}]$ abundances higher than the pure r -process value (green solid line in Figure 8), indicating a heterogeneous mixture of r - and s - processes. Star #9 and star #47 show $[\text{Ba}/\text{Eu}]$ abundances close to the pure r -process value, indicating a strong r -process contribution.

4. DISCUSSION

4.1. Chemical similarity between N-rich field stars and GC stars

Though our sample stars have been confirmed to be mostly N-rich using CN-CH features around 4000 Å ([Paper I](#)), further chemical tagging with more elements requires high-resolution spectra. Using the MIKE and APOGEE spectra, we find that most N-rich field stars show consistent Na, O, Mg, Al, Si, and Ca with GC stars of similar metallicities. This chemical similar-

ity supports the GC origin of these N-rich field stars. Two stars with strong Mg-depletion are also found. Strong Mg-depletion is usually found in very metal-poor ($[\text{Fe}/\text{H}] < -2.0$) GCs (e.g., M15, M92). Two N-rich field stars show strong Mg-depletion at $[\text{Fe}/\text{H}] \sim -1.3$ is somewhat puzzling. One possible scenario is: accreted materials from companion stars may change the Mg abundances of these two N-rich field stars dramatically ([Fernández-Trincado et al. 2017](#)).

Based on the Na abundances, we find that most N-rich field stars are located in the transition region between FG and SG stars, thus it is difficult to verify their SG origin (see Figure 1). On the other hand, the Mg-Al figure (Figure 2) shows that half of our sample have $[\text{Al}/\text{Fe}] > 0.5$, which is largely different than GC FG stars. Interestingly, [Fernández-Trincado et al. \(2020\)](#) identified 29 mildly metal-poor ($[\text{Fe}/\text{H}] < -0.7$) field

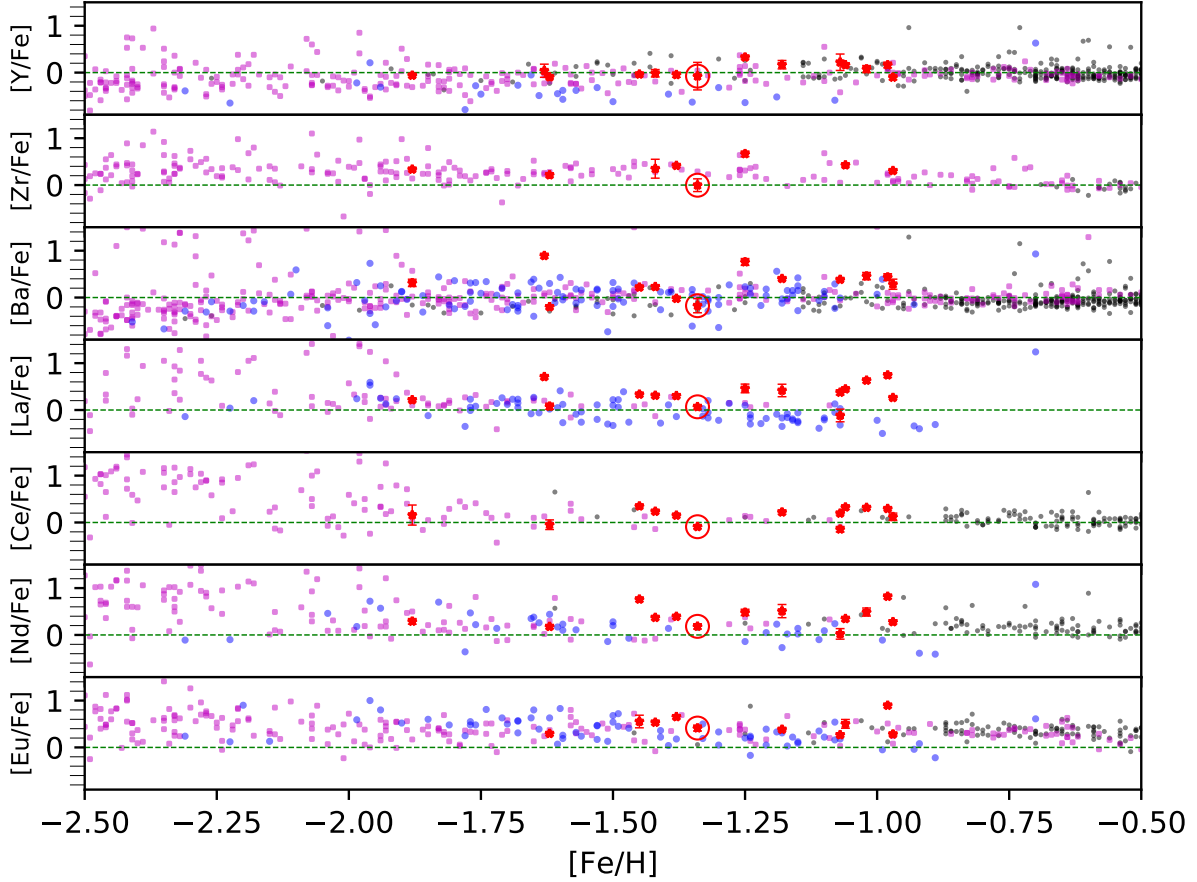


Figure 6. Abundances of neutron capture elements vs. $[\text{Fe}/\text{H}]$. Symbols are same as Figure 5.

stars with $[\text{Al}/\text{Fe}] > 0.5$. They suggested that these stars were ejected into the bulge and inner halo from GCs formed in situ and/or GCs formed in dissolved dwarf galaxy progenitors.

4.2. *In situ or ex situ?*

As our understanding of the MW formation rapidly improves in the *Gaia* era, GCs are now believed to formed in both MW and dwarf satellite galaxies, and later merged together as the current Galactic GCs (e.g., Massari et al. 2019; Myeong et al. 2019). GCs formed in situ and ex situ tend to show different chemical and dynamical signatures. If the N-rich field stars were escaped from GCs, they should carry similar chemo-dynamical information as the host GCs. Paper II showed that our parent N-rich field sample (~ 100) have both stars formed in situ and stars formed ex situ using kinematics. In this work, one interesting star (star #9, large circles in Figures 4 and 5) show consistently low $[\text{Mg}/\text{Fe}]$, $[\text{Si}/\text{Fe}]$, $[\text{Ca}/\text{Fe}]$, $[\text{Ti}/\text{Fe}]$, $[\text{Sc}/\text{Fe}]$, $[\text{V}/\text{Fe}]$, and $[\text{Co}/\text{Fe}]$

compared to MW stars at similar metallicities, which is a strong evidence that this star was formed in dissolved dwarf galaxies. The relatively higher $[\text{Al}/\text{Fe}]$ of star #9 compared to dwarf galaxy field stars indicates that it is possibly enriched in GC environment, as Al-rich stars can be found in accreted GCs. On the other hand, stars with $-1.25 \leq [\text{Fe}/\text{H}] \leq -0.95$ show $[\alpha/\text{Fe}]$ and iron-peak abundances consistent with other MW field stars, indicating that they were formed in situ. Moreover, we checked their kinematic information in Paper II, and found that star #9 shows $\langle E \rangle$ and $\langle Lz \rangle$ consistent with *Gaia*-Sausage-Enceladus (GSE) stars (Figure 9), while stars with $-1.25 \leq [\text{Fe}/\text{H}] \leq -0.95$ show in situ disk or halo kinematics (e.g. Naidu et al. 2020). Interestingly, star #9 shows $[\text{Ba}/\text{Eu}]$ close to the r-process limit, which is consistent with other GSE stars observed in Aguado et al. (2020). This is a straightforward example to demonstrate that chemical tagging is possible to help decipher the origin of field stars. We also ac-

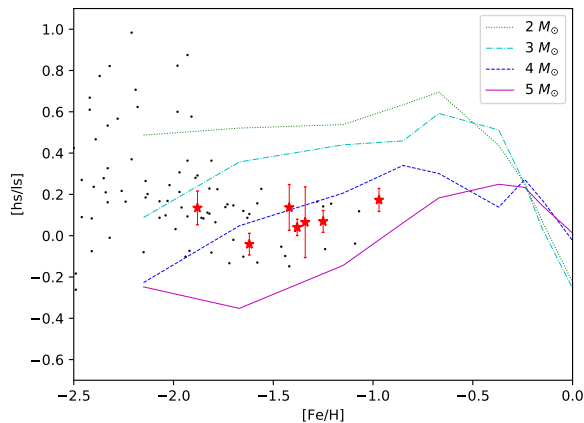


Figure 7. $[\text{hs/ls}]$ vs. $[\text{Fe/H}]$. Abundances of N-rich stars are shown as red stars, while black dots correspond to Milky Way stars from halo and disc (same sources as black dots in Figure 2). The grid lines with different colors and line styles indicate stars enriched by AGB stars of different masses (Cristallo et al. 2015).

knowledge the difficulties in judging the origin of field stars based on several chemical and dynamical observation evidences, which are not always consistent with each other. A more sophisticated probability estimation of their origin is left for further studies.

5. CONCLUSIONS

We used MIKE spectra of 15 stars, which are selected from the LAMOST N-rich field star sample, to analyse their chemical abundances for more than 20 elements. We find that the Na, O, Mg, Al, Si, and Ca abundances of the N-rich field stars are consistent with GC stars, which supports their GC origin. Given that GC FG and SG stars have large overlap in Na-O and Mg-Al parameter space, it is difficult to confirm the SG origin

of N-rich field stars. But we do find seven stars with $[\text{Al/Fe}] > 0.5$, which is typical for GC SG stars.

We notice that one star (#9) with consistently low $[\text{Mg/Fe}]$, $[\text{Si/Fe}]$, $[\text{Ca/Fe}]$, $[\text{Ti/Fe}]$, $[\text{Sc/Fe}]$, $[\text{V/Fe}]$, and $[\text{Co/Fe}]$ show similar kinematic and $[\text{Ba/Eu}]$ as other stars from GSE. On the other hand, more metal-rich stars ($-1.25 \leq [\text{Fe/H}] \leq -0.95$) show α -elements abundances and iron-peak abundances more consistent with MW field stars rather than dwarf galaxies, indicating likely in situ origin.

The ratio between heavy s-process elements and light s-process elements reveals that most N-rich field stars could be enriched by AGB stars with masses around 3–5 M_{\odot} . A detailed comparison between different chemical models and the obtained chemical patterns of our N-rich field stars would be fruitful for future discussion (e.g., Masseron et al. 2020).

ACKNOWLEDGMENTS

We thank Ian Thompson, Yang Huang for helpful discussions. We thank the anonymous referee for insightful comments. J.Y. and B.T. gratefully acknowledges support from the National Natural Science Foundation of China under grant No. U1931102. D.G. gratefully acknowledges support from the Chilean Centro de Excelencia en Astrofísica y Tecnologías Afines (CATA) BASAL grant AFB-170002. D.G. also acknowledges financial support from the Dirección de Investigación y Desarrollo de la Universidad de La Serena through the Programa de Incentivo a la Investigación de Académicos (PIA-DIDULS). Guoshoujing Telescope (the Large Sky Area Multi-Object Fiber Spectroscopic Telescope LAMOST) is a National Major Scientific Project built by the Chinese Academy of Sciences. Funding for the project has been provided by the National Development and Reform Commission. LAMOST is operated and managed by the National Astronomical Observatories, Chinese Academy of Sciences.

REFERENCES

- Aguado, D. S., Belokurov, V., Myeong, G. C., et al. 2020, arXiv e-prints, arXiv:2012.01430.
<https://arxiv.org/abs/2012.01430>
- Arnould, M., Goriely, S., & Jorissen, A. 1999, *A&A*, 347, 572
- Barklem, P. S., Christlieb, N., Beers, T. C., et al. 2005, *A&A*, 439, 129, doi: [10.1051/0004-6361:20052967](https://doi.org/10.1051/0004-6361/20052967)
- Bastian, N., & Lardo, C. 2018, *ARA&A*, 56, 83, doi: [10.1146/annurev-astro-081817-051839](https://doi.org/10.1146/annurev-astro-081817-051839)
- Bekki, K., Jeřábková, T., & Kroupa, P. 2017, *MNRAS*, 471, 2242, doi: [10.1093/mnras/stx1609](https://doi.org/10.1093/mnras/stx1609)
- Bensby, T., Feltzing, S., & Oey, M. S. 2014, *A&A*, 562, A71, doi: [10.1051/0004-6361/201322631](https://doi.org/10.1051/0004-6361/201322631)
- Bernstein, R., Shectman, S. A., Gunnels, S. M., Mochnacki, S., & Athey, A. E. 2003, in *Society of Photo-Optical Instrumentation Engineers (SPIE) Conference Series*, Vol. 4841, *Instrument Design and Performance for Optical/Infrared Ground-based Telescopes*, ed. M. Iye & A. F. M. Moorwood, 1694–1704, doi: [10.1117/12.461502](https://doi.org/10.1117/12.461502)
- Bisterzo, S., Travaglio, C., Gallino, R., Wiescher, M., & Käppeler, F. 2014, *ApJ*, 787, 10, doi: [10.1088/0004-637X/787/1/10](https://doi.org/10.1088/0004-637X/787/1/10)

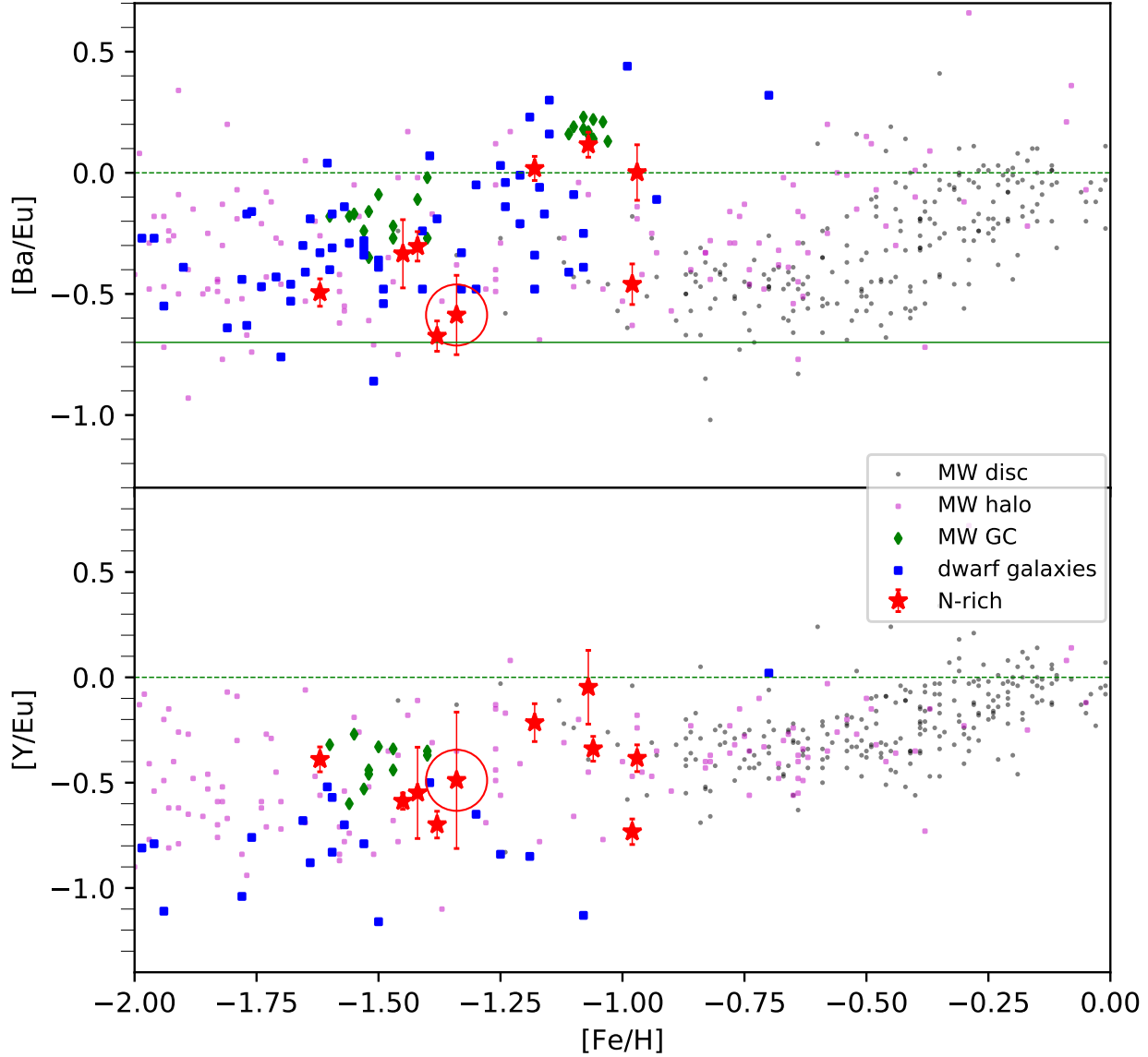


Figure 8. $[\text{Ba}/\text{Eu}]$ vs. $[\text{Fe}/\text{H}]$ and $[\text{Y}/\text{Eu}]$ vs. $[\text{Fe}/\text{H}]$. Abundances of N-rich stars are shown as red stars. Magenta squares correspond to MW halo stars, while black dots correspond to MW disc stars. The green solid line indicates that a typical value of a pure r -process by (Bisterzo et al. 2014). Green diamonds correspond to MW GCs (McWilliam et al. 1992; James et al. 2004; Muñoz et al. 2013; Johnson et al. 2017; Massari et al. 2017). Blue squares correspond to dwarf galaxies from Sagittarius (Hasselquist et al. 2017), Sculptor (Hill et al. 2019) (for $[\text{Ba}/\text{Eu}]$), Carina (Venn et al. 2012), and 19 red giants from Sagittarius, Fornax, Carina, Leo I (Shetrone et al. 2003). Star #9 with high extragalactic GC origin possibility are labeled with large red circle.

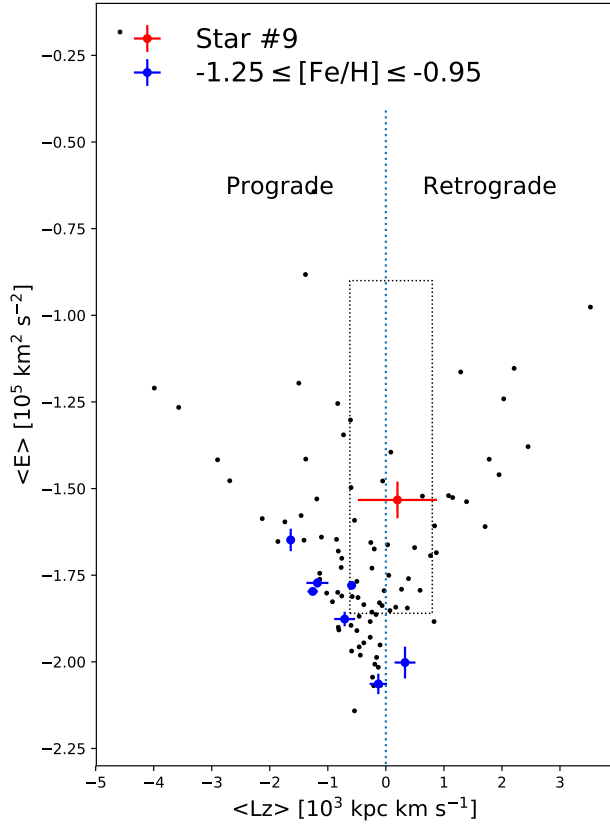


Figure 9. Mean z -direction angular momentum $\langle L_z \rangle$ vs. mean orbital energy $\langle E \rangle$. Star #9 is labelled as red dots with error bars, while stars with $-1.25 \leq [\text{Fe}/\text{H}] \leq -0.95$ are labelled as blue dots with error bars. The dotted rectangle shows the GSE region^a given by [Massari et al. \(2019\)](#).

^a Positive $\langle L_z \rangle$ indicate retrograde and negative $\langle L_z \rangle$ indicate prograde, which is the opposite in [Massari et al. \(2019\)](#). This is related to the Galactocentric coordinate system that we used ([Paper II](#)).

- Busso, M., Gallino, R., Lambert, D. L., Travaglio, C., & Smith, V. V. 2001, *ApJ*, 557, 802, doi: [10.1086/322258](#)
- Carretta, E., & Bragaglia, A. 2020, arXiv e-prints, arXiv:2011.08208. <https://arxiv.org/abs/2011.08208>
- Carretta, E., Bragaglia, A., Gratton, R., & Lucatello, S. 2009a, *A&A*, 505, 139, doi: [10.1051/0004-6361/200912097](#)
- Carretta, E., Bragaglia, A., Gratton, R., et al. 2010a, *ApJL*, 712, L21, doi: [10.1088/2041-8205/712/1/L21](#)
- Carretta, E., Bragaglia, A., Gratton, R. G., et al. 2010b, *A&A*, 516, A55, doi: [10.1051/0004-6361/200913451](#)
- . 2009b, *A&A*, 505, 117, doi: [10.1051/0004-6361/200912096](#)
- Cayrel, R., Depagne, E., Spite, M., et al. 2004, *A&A*, 416, 1117, doi: [10.1051/0004-6361:20034074](#)
- Conroy, C. 2012, *ApJ*, 758, 21, doi: [10.1088/0004-637X/758/1/21](#)
- Côté, B., Fryer, C. L., Belczynski, K., et al. 2018, *ApJ*, 855, 99, doi: [10.3847/1538-4357/aaad67](#)
- Cristallo, S., Straniero, O., Piersanti, L., & Gobrecht, D. 2015, *ApJS*, 219, 40, doi: [10.1088/0067-0049/219/2/40](#)
- Dalessandro, E., Massari, D., Bellazzini, M., et al. 2014, *ApJL*, 791, L4, doi: [10.1088/2041-8205/791/1/L4](#)
- D’Ercole, A., Vesperini, E., D’Antona, F., McMillan, S. L. W., & Recchi, S. 2008, *MNRAS*, 391, 825, doi: [10.1111/j.1365-2966.2008.13915.x](#)
- Fernández-Trincado, J. G., Beers, T. C., Minniti, D., et al. 2020, *A&A*, 643, L4, doi: [10.1051/0004-6361/202039207](#)
- Fernández-Trincado, J. G., Beers, T. C., Tang, B., et al. 2019, *MNRAS*, 488, 2864, doi: [10.1093/mnras/stz1848](#)
- Fernández-Trincado, J. G., Robin, A. C., Moreno, E., et al. 2016, *ApJ*, 833, 132, doi: [10.3847/1538-4357/833/2/132](#)
- Fernández-Trincado, J. G., Zamora, O., García-Hernández, D. A., et al. 2017, *ApJL*, 846, L2, doi: [10.3847/2041-8213/aa8032](#)
- Fulbright, J. P. 2000, *AJ*, 120, 1841, doi: [10.1086/301548](#)
- González Hernández, J. I., & Bonifacio, P. 2009, *A&A*, 497, 497, doi: [10.1051/0004-6361/200810904](#)
- Gratton, R. G., Carretta, E., & Bragaglia, A. 2012, *A&A Rv*, 20, 50, doi: [10.1007/s00159-012-0050-3](#)
- Hasselquist, S., Shetrone, M., Smith, V., et al. 2017, *ApJ*, 845, 162, doi: [10.3847/1538-4357/aa7ddc](#)
- Hayes, C. R., Majewski, S. R., Hasselquist, S., et al. 2020, *ApJ*, 889, 63, doi: [10.3847/1538-4357/ab62ad](#)
- Hill, V., Skúladóttir, Á., Tolstoy, E., et al. 2019, *A&A*, 626, A15, doi: [10.1051/0004-6361/201833950](#)
- Horta, D., Schiavon, R. P., Mackereth, J. T., et al. 2020, *MNRAS*, 493, 3363, doi: [10.1093/mnras/staa478](#)
- James, G., François, P., Bonifacio, P., et al. 2004, *A&A*, 414, 1071, doi: [10.1051/0004-6361:20034014](#)
- Johnson, C. I., Caldwell, N., Rich, R. M., et al. 2017, *ApJ*, 842, 24, doi: [10.3847/1538-4357/aa7414](#)
- Jönsson, H., Holtzman, J. A., Allende Prieto, C., et al. 2020, *AJ*, 160, 120, doi: [10.3847/1538-3881/aba592](#)
- Kajino, T., Aoki, W., Balantekin, A. B., et al. 2019, *Progress in Particle and Nuclear Physics*, 107, 109, doi: [10.1016/j.pnpnp.2019.02.008](#)
- Karakas, A. I., & Lattanzio, J. C. 2014, *PASA*, 31, e030, doi: [10.1017/pasa.2014.21](#)
- Kelson, D. D. 2003, *PASP*, 115, 688, doi: [10.1086/375502](#)
- Kelson, D. D., Illingworth, G. D., van Dokkum, P. G., & Franx, M. 2000, *ApJ*, 531, 137, doi: [10.1086/308460](#)
- Kobayashi, C., Karakas, A. I., & Lugaro, M. 2020, *ApJ*, 900, 179, doi: [10.3847/1538-4357/abae65](#)
- Koch, A., Grebel, E. K., & Martell, S. L. 2019, *A&A*, 625, A75, doi: [10.1051/0004-6361/201834825](#)

- Lamers, H. J. G. L. M., Baumgardt, H., & Gieles, M. 2010, MNRAS, 409, 305, doi: [10.1111/j.1365-2966.2010.17309.x](https://doi.org/10.1111/j.1365-2966.2010.17309.x)
- Lardo, C., Bellazzini, M., Pancino, E., et al. 2011, A&A, 525, A114, doi: [10.1051/0004-6361/201015662](https://doi.org/10.1051/0004-6361/201015662)
- Larsen, S. S., Baumgardt, H., Bastian, N., et al. 2015, ApJ, 804, 71, doi: [10.1088/0004-637X/804/1/71](https://doi.org/10.1088/0004-637X/804/1/71)
- Lim, D., Lee, Y.-W., Pasquato, M., Han, S.-I., & Roh, D.-G. 2016, ApJ, 832, 99, doi: [10.3847/0004-637X/832/2/99](https://doi.org/10.3847/0004-637X/832/2/99)
- Majewski, S. R., Schiavon, R. P., Frinchaboy, P. M., et al. 2017, AJ, 154, 94, doi: [10.3847/1538-3881/aa784d](https://doi.org/10.3847/1538-3881/aa784d)
- Martell, S. L., & Grebel, E. K. 2010, A&A, 519, A14, doi: [10.1051/0004-6361/201014135](https://doi.org/10.1051/0004-6361/201014135)
- Martell, S. L., Smolinski, J. P., Beers, T. C., & Grebel, E. K. 2011, A&A, 534, A136, doi: [10.1051/0004-6361/201117644](https://doi.org/10.1051/0004-6361/201117644)
- Martell, S. L., Shetrone, M. D., Lucatello, S., et al. 2016, ApJ, 825, 146, doi: [10.3847/0004-637X/825/2/146](https://doi.org/10.3847/0004-637X/825/2/146)
- Massari, D., Koppelman, H. H., & Helmi, A. 2019, A&A, 630, L4, doi: [10.1051/0004-6361/201936135](https://doi.org/10.1051/0004-6361/201936135)
- Massari, D., Mucciarelli, A., Dalessandro, E., et al. 2017, MNRAS, 468, 1249, doi: [10.1093/mnras/stx549](https://doi.org/10.1093/mnras/stx549)
- Masseron, T., García-Hernández, D. A., Zamora, O., & Manchado, A. 2020, ApJL, 904, L1, doi: [10.3847/2041-8213/abc6ac](https://doi.org/10.3847/2041-8213/abc6ac)
- Masseron, T., Merle, T., & Hawkins, K. 2016, BACCHUS: Brussels Automatic Code for Characterizing High accuracy Spectra. <http://ascl.net/1605.004>
- Matteucci, F., & Greggio, L. 1986, A&A, 154, 279
- McWilliam, A. 1998, AJ, 115, 1640, doi: [10.1086/300289](https://doi.org/10.1086/300289)
- McWilliam, A., Geisler, D., & Rich, R. M. 1992, PASP, 104, 1193, doi: [10.1086/133108](https://doi.org/10.1086/133108)
- Mészáros, S., Masseron, T., García-Hernández, D. A., et al. 2020, MNRAS, 492, 1641, doi: [10.1093/mnras/stz3496](https://doi.org/10.1093/mnras/stz3496)
- Miholics, M., Webb, J. J., & Sills, A. 2015, MNRAS, 454, 2166, doi: [10.1093/mnras/stv2086](https://doi.org/10.1093/mnras/stv2086)
- Milone, A. P., Piotto, G., Renzini, A., et al. 2017, MNRAS, 464, 3636, doi: [10.1093/mnras/stw2531](https://doi.org/10.1093/mnras/stw2531)
- Muñoz, C., Geisler, D., & Villanova, S. 2013, MNRAS, 433, 2006, doi: [10.1093/mnras/stt868](https://doi.org/10.1093/mnras/stt868)
- Myeong, G. C., Vasiliev, E., Iorio, G., Evans, N. W., & Belokurov, V. 2019, MNRAS, 488, 1235, doi: [10.1093/mnras/stz1770](https://doi.org/10.1093/mnras/stz1770)
- Naidu, R. P., Conroy, C., Bonaca, A., et al. 2020, ApJ, 901, 48, doi: [10.3847/1538-4357/abaef4](https://doi.org/10.3847/1538-4357/abaef4)
- Nomoto, K., Iwamoto, K., Nakasato, N., et al. 1997, Nuclear Physics A, 621, 467, doi: [10.1016/S0375-9474\(97\)00291-1](https://doi.org/10.1016/S0375-9474(97)00291-1)
- Pancino, E., Romano, D., Tang, B., et al. 2017, A&A, 601, A112, doi: [10.1051/0004-6361/201730474](https://doi.org/10.1051/0004-6361/201730474)
- Piotto, G., Milone, A. P., Bedin, L. R., et al. 2015, AJ, 149, 91, doi: [10.1088/0004-6256/149/3/91](https://doi.org/10.1088/0004-6256/149/3/91)
- Reddy, B. E., Lambert, D. L., & Allende Prieto, C. 2006, MNRAS, 367, 1329, doi: [10.1111/j.1365-2966.2006.10148.x](https://doi.org/10.1111/j.1365-2966.2006.10148.x)
- Reddy, B. E., Tomkin, J., Lambert, D. L., & Allende Prieto, C. 2003, MNRAS, 340, 304, doi: [10.1046/j.1365-8711.2003.06305.x](https://doi.org/10.1046/j.1365-8711.2003.06305.x)
- Roederer, I. U., Preston, G. W., Thompson, I. B., et al. 2014, AJ, 147, 136, doi: [10.1088/0004-6256/147/6/136](https://doi.org/10.1088/0004-6256/147/6/136)
- Schaerer, D., & Charbonnel, C. 2011, MNRAS, 413, 2297, doi: [10.1111/j.1365-2966.2011.18304.x](https://doi.org/10.1111/j.1365-2966.2011.18304.x)
- Schiavon, R. P., Zamora, O., Carrera, R., et al. 2017, MNRAS, 465, 501, doi: [10.1093/mnras/stw2162](https://doi.org/10.1093/mnras/stw2162)
- Shetman, S. A., & Johns, M. 2003, in Society of Photo-Optical Instrumentation Engineers (SPIE) Conference Series, Vol. 4837, Large Ground-based Telescopes, ed. J. M. Oschmann & L. M. Stepp, 910–918, doi: [10.1117/12.457909](https://doi.org/10.1117/12.457909)
- Shetrone, M., Venn, K. A., Tolstoy, E., et al. 2003, AJ, 125, 684, doi: [10.1086/345966](https://doi.org/10.1086/345966)
- Simioni, M., Milone, A. P., Bedin, L. R., et al. 2016, MNRAS, 463, 449, doi: [10.1093/mnras/stw2003](https://doi.org/10.1093/mnras/stw2003)
- Tang, B., Fernández-Trincado, J. G., Liu, C., et al. 2020, ApJ, 891, 28, doi: [10.3847/1538-4357/ab7233](https://doi.org/10.3847/1538-4357/ab7233)
- Tang, B., Liu, C., Fernández-Trincado, J. G., et al. 2019, ApJ, 871, 58, doi: [10.3847/1538-4357/aaf6b1](https://doi.org/10.3847/1538-4357/aaf6b1)
- Tang, B., Geisler, D., Friel, E., et al. 2017, A&A, 601, A56, doi: [10.1051/0004-6361/201629883](https://doi.org/10.1051/0004-6361/201629883)
- Tang, B., Fernández-Trincado, J. G., Geisler, D., et al. 2018, ApJ, 855, 38, doi: [10.3847/1538-4357/aaaaea](https://doi.org/10.3847/1538-4357/aaaaea)
- Thielemann, F.-K., Arcones, A., Käppeli, R., et al. 2011, Progress in Particle and Nuclear Physics, 66, 346, doi: [10.1016/j.pnpnp.2011.01.032](https://doi.org/10.1016/j.pnpnp.2011.01.032)
- Vanderbeke, J., De Propris, R., De Rijcke, S., et al. 2015, MNRAS, 451, 275, doi: [10.1093/mnras/stv928](https://doi.org/10.1093/mnras/stv928)
- Venn, K. A., Shetrone, M. D., Irwin, M. J., et al. 2012, ApJ, 751, 102, doi: [10.1088/0004-637X/751/2/102](https://doi.org/10.1088/0004-637X/751/2/102)
- Watson, D., Hansen, C. J., Selsing, J., et al. 2019, Nature, 574, 497, doi: [10.1038/s41586-019-1676-3](https://doi.org/10.1038/s41586-019-1676-3)
- Woosley, S. E., & Weaver, T. A. 1995, ApJS, 101, 181, doi: [10.1086/192237](https://doi.org/10.1086/192237)
- Woosley, S. E., Wilson, J. R., Mathews, G. J., Hoffman, R. D., & Meyer, B. S. 1994, ApJ, 433, 229, doi: [10.1086/174638](https://doi.org/10.1086/174638)
- Yong, D., Norris, J. E., Bessell, M. S., et al. 2013, ApJ, 762, 26, doi: [10.1088/0004-637X/762/1/26](https://doi.org/10.1088/0004-637X/762/1/26)
- Zhao, G., Zhao, Y.-H., Chu, Y.-Q., Jing, Y.-P., & Deng, L.-C. 2012, Research in Astronomy and Astrophysics, 12, 723, doi: [10.1088/1674-4527/12/7/002](https://doi.org/10.1088/1674-4527/12/7/002)

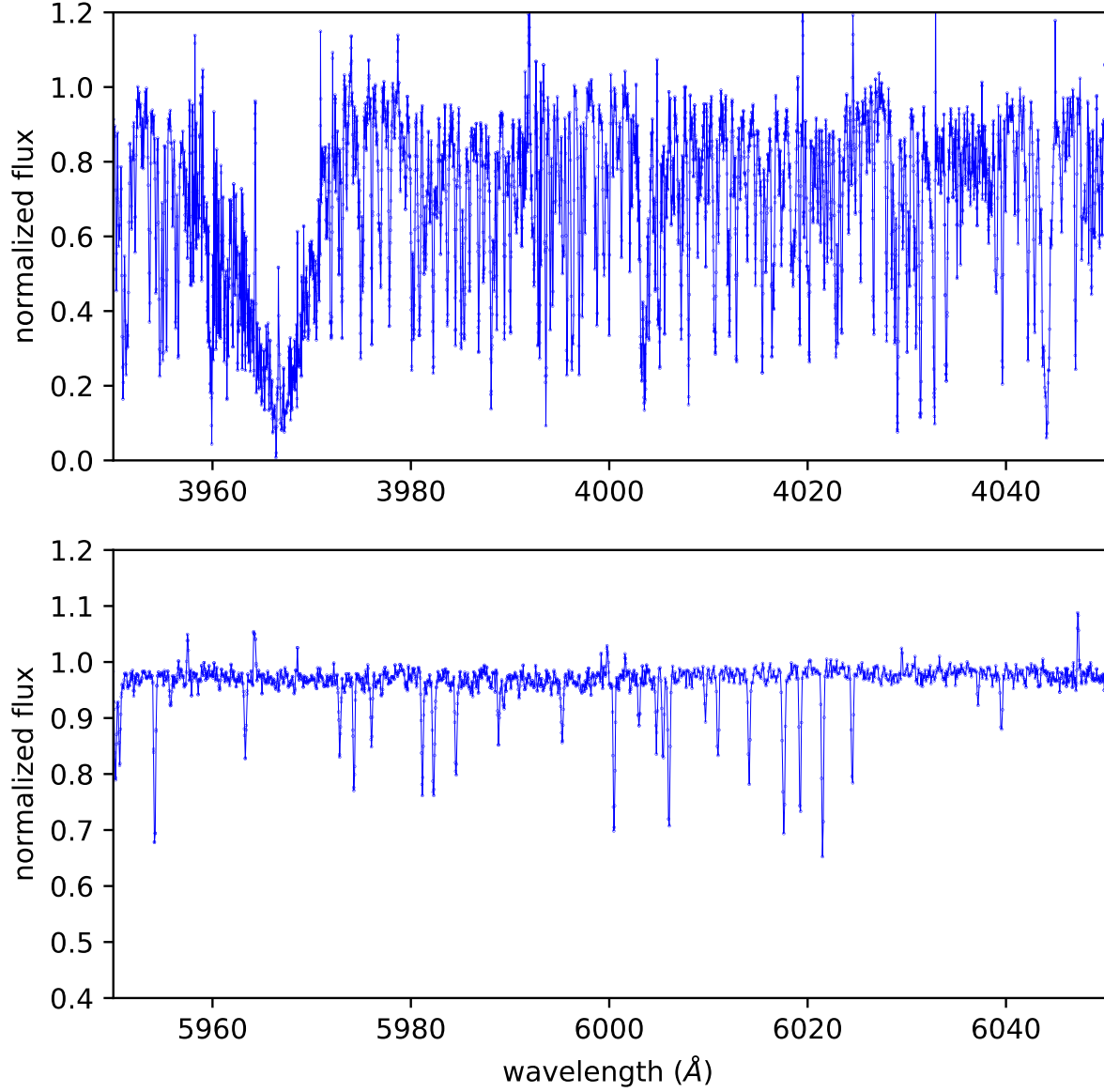


Figure 10. Spectra of star #88 of both blue side and red side.

APPENDIX

Spectra of star #88 of both blue side (3950 – 4050 Å) and red side (5950 – 6050 Å) are shown in Figure 10. We adopt red side spectra ($\lambda > 5000$ Å) in abundances determination when considering their better SNR. T_{eff} is determined by obtaining null trend for the abundance of iron lines against excitation potential is shown in Figure 11. An example of abundances determination with four different methods is shown in Figure 12 as mentioned in Section 2.

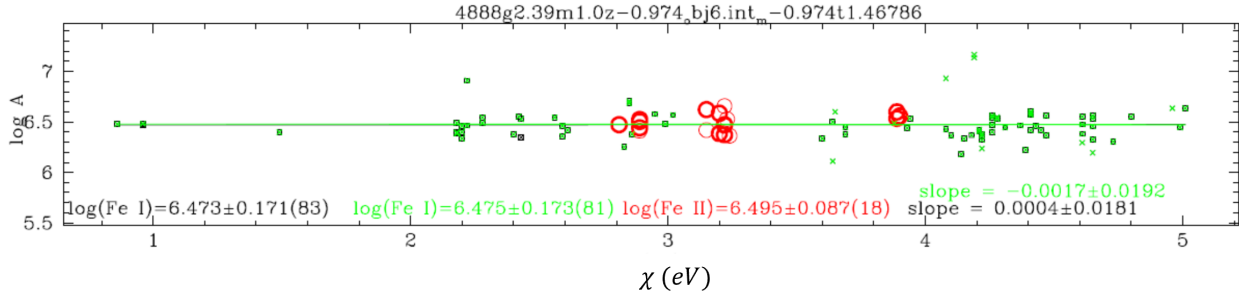


Figure 11. Illustration of T_{eff} determination with iron abundances and excitation potential.

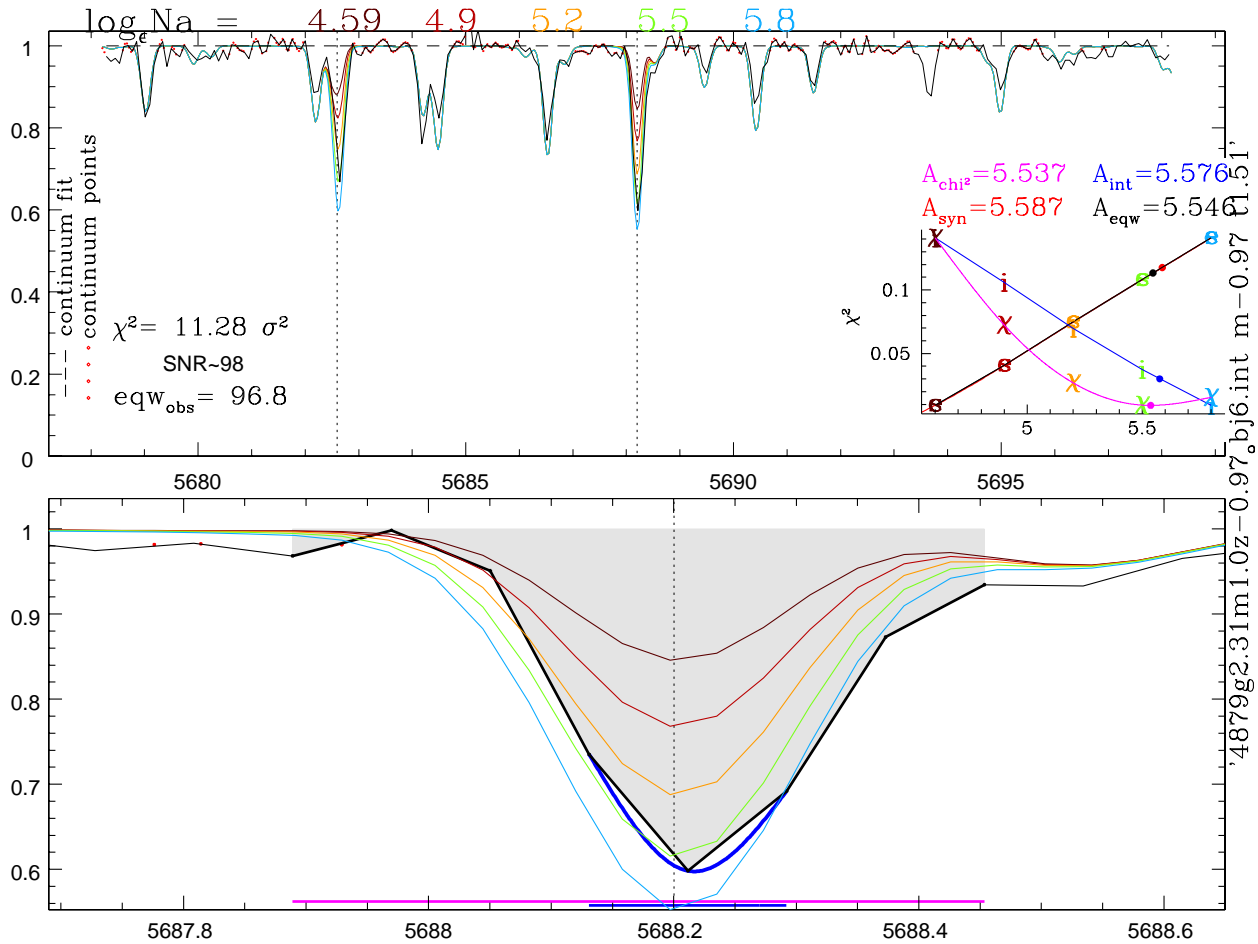


Figure 12. Comparison of four different methods (χ^2 minimization, line intensity, equivalent width, and spectral synthesis) in determining Na abundances for star #88. The black solid line shows the observed normalized spectrum, while colored lines show synthesis obtained by different methods in both upper and bottom panel. The inserted panel in the bottom right corner of the upper panel shows the diagram for the four methods for abundances determination. Each of the method is represented by a different color (χ^2 minimization: magenta, line intensity: blue, equivalent width: black, spectral synthesis: red). (See more detailed descriptions in (Masseron *et al.* 2016).)